THE JOURNAL OF PHYSICAL CHEMISTRY C
A JOURNAL OF THE AMERICAN CHEMICAL SOCIETY

pubs.acs.org/JPCC
Article

Toward High-Efficiency Solar Cells: Insights into $AsNCa_3$ Antiperovskite as an Active Layer

Muhammad Irfan, Bill D. Aparicio-Huacarpuma, Carlos M. de Oliveira Bastos, Celso R. C. Rêgo, Diego Guedes-Sobrinho, Rafael Besse, Maurício J. Piotrowski, Alysson M. Almeida Silva, Alexandre C. Dias,* and L. A. Ribeiro, Jr.

Cite This: https://doi.org/10.1021/acs.jpcc.5c05620

Read Online

ACCESS | Metrics & More | Article Recommendations | Supporting Information

ABSTRACT: Advances in photovoltaic technology are a viable route for contributing to cleaner and more sustainable energy solutions, placing perovskite-based materials among the best candidates for solar energy conversion. However, some challenges must be addressed to enhance their performance and stability. Herein, we report an investigation of the $AsNCa_3$ antiperovskite system for its potential in photovoltaic devices, using the density functional theory with semilocal and hybrid exchange−correlation functionals. We consider eight distinct crystalline phases, their structural parameters, dynamical stability, and electronic and optical properties. Furthermore, we consider each structural phase's contributions to solar harvesting efficiency by calculating the power conversion efficiency (PCE) using the spectroscopic limited maximum efficiency formalism, which in this case reaches a maximum of 31.2%. All dynamically stable phases exhibit a band gap around ∼1.3 eV, which lies within the optimal range for single-junction solar cells and yields PCE values comparable to the theoretical maximum PCE for silicon. These results place $AsNCa_3$ antiperovskite as promising candidate for high-efficiency photovoltaic applications. Notably, the PCE is only slightly changed by structural phase modification, suggesting that phase transitions induced by environmental conditions during device operation might not compromise the device performance.

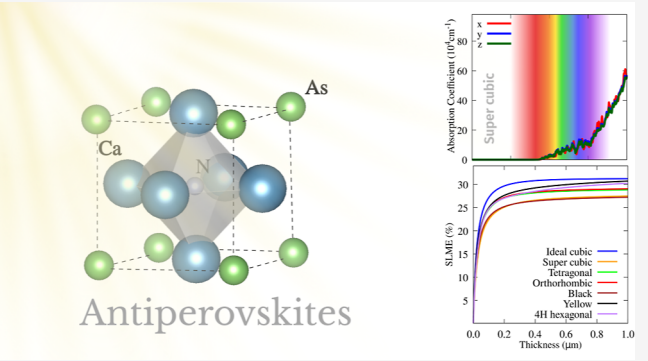

1. INTRODUCTION

Solar energy promises to address the increasing global demand for electricity by harnessing photovoltaic (PV) technologies that convert direct sunlight into electric energy.[1,2] Of all the materials used in PV devices, halide perovskites are exceptional through their high absorption coefficient, long carrier diffusion length, and low-cost processing, among other benefits.[3,4] At the same time, however, regardless of the very high power conversion efficiencies that these materials, including organic−inorganic metal halide perovskites (MHPs),[5,6] are capable of, there exist several significant challenges. Among them are (i) thermal and moisture instability;[7,8] (ii) sensitivity to ultraviolet radiation;[9,10] (iii) chemical degradation by exposure to oxygen, water, and other species;[11−13] (iv) toxicity, as most of the efficient MHPs are lead-based [e.g., $MAPbI_3$, $CsPbI_3$, $Cs_2PbI_2Cl_2$, and $(BA)_n(MA)_{n-1}PbI_4$];[8,10,14−17] (v) ion migration, wherein mobile species such as iodide and methylammonium migrate under electric fields or light exposure, causing changes in the structure and loss of efficiency.[18−20] Expanding the knowledge on chemically and structurally related materials becomes vital for overcoming these limitations.

The cubic phase of α-$CsPbI_3$, one of the most representative all-inorganic MHPs, has been widely investigated, given its band gap close to 1.70 eV, which fits well within the optimal range for single-junction solar cells.[21−23] However, stabilizing this cubic phase at ambient conditions remains a challenge,[24−26] since at room temperature, it spontaneously transforms into an orthorhombic phase (δ-$CsPbI_3$, namely, yellow phase) with a much larger band gap of 2.82 eV, i.e., the absorption spectrum is shifted toward the ultraviolet region.[27,28] In this context, beyond thermodynamic strategies such as pressure-induced stabilization,[29,30] manipulating the composition of ABX_3 represents a practical approach to correlate phase stability with desirable optoelectronic properties.[8,10,15,16]

Another perovskite-related family of materials, the antiperovskites, has also attracted notable interest in recent years

Received: August 11, 2025
Revised: September 3, 2025
Accepted: September 4, 2025

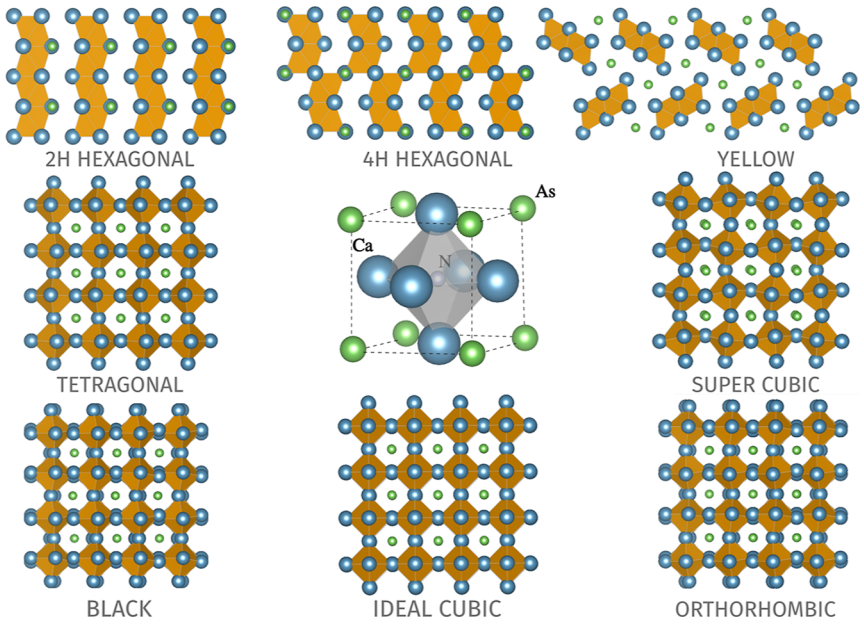

Figure 1. Structural representations of the eight $AsNCa_3$ antiperovskite polymorphs investigated in this work. Octahedral frameworks are highlighted to emphasize symmetry variations and distortions across different crystalline phases.

due to their respective sets of novel properties, including superconductivity,[31] giant magnetoresistance,[32] and zero or negative thermal expansion.[33] Antiperovskites are characterized by the reversal of the A and X site occupancies of the classical perovskite structure, but still retaining the exact ideal cubic space group symmetry ($Pm\bar{3}m$).[1,34−36] Perhaps the most fascinating of these materials is $AsNCa_3$ due to its tunable band structures and likely topological character.[37] Additionally, its thermoelectric, piezoelectric,[38] photovoltaic application,[39,40] and charge transport behavior[41] are highly desirable for future energy applications and quantum devices.

Here, we investigate the photovoltaic (PV) potential of antiperovskite $AsNCa_3$ using first-principles calculations. We systematically study its structural, electronic, and optical properties by advancing across eight different polymorphs:[36] cubic, black, orthorhombic, yellow, hexagonal (2H and 4H), tetragonal, and a so-called supercubic phase,[36] which provides a more realistic description of the cubic phase (a realistic distortion of the ideal cubic structure). Thus, the main idea is to understand how structural variations influence the material's light-harvesting performance and to identify promising phase configurations for photovoltaic applications.

2. METHODOLOGY

We performed density functional theory (DFT) calculations using the Vienna ab initio simulation package (VASP),[42,43] solving the Kohn−Sham equations[44,45] via the projector augmented-wave (PAW) method.[46] The exchange−correlation energy was initially described using the Perdew−Burke−Ernzerhof (PBE) semilocal functional.[47] To compensate for the well-known underestimation of band gaps by local and semilocal functionals, which is attributable to self-interaction and derivative discontinuity errors,[48,49] we employed the HSE06 screened hybrid functional,[50,51] which typically reduces band gap discrepancies for common semiconductors.[52,53] The structural optimization was conducted by relaxing both the stress tensor and atomic forces, with a plane-wave cutoff energy of 800 eV and a **k**-point density equivalent to 40 $Å^{-1}$. Convergence thresholds were set at 10^{-6} eV for the total energy and 0.010 eV/Å for atomic forces. All subsequent calculations used a cutoff of 450 eV, while density of states (DOS) calculations employed a refined **k**-point density of 80 $Å^{-1}$.

Dynamical stability was assessed via phonon dispersion calculations at 0 K using the Phonopy package[54] in combination with the DFTB+ code,[55] based on the extended tight-binding method (xTB)[56] with GFN1-xTB parametrization.[57,58] For these calculations, the crystal structure was also optimized with DFTB+; the results are closer to those obtained with DFT, validating the approximation. This hybrid approach reproduces phonon frequencies at a computational cost lower than that of standard DFT phonon calculations. We used a **k**-point density of 40 $Å^{-1}$, with $3 \times 3 \times 3$ supercells for the cubic phase and $2 \times 2 \times 2$ supercells for all other phases to capture long-range interactions efficiently.

Optical absorption spectra were computed within the independent-particle approximation (IPA) using WanTiBEXOS.[59] The calculations rely on a maximally localized Wannier function tight-binding Hamiltonian extracted from DFT-HSE06 calculations via the Wannier90 code,[60] with s-, p- and d- orbital projections for As and Ca, and p-orbital projections for N. Full parameter details are provided in Section S10, Table S5, of the Supporting Information. Finally, we evaluated the power conversion efficiency (PCE) using the spectroscopic limited maximum efficiency (SLME) framework,[61] assuming the AM 1.5G solar spectrum[62] and device operation at 300 K. The PCE is calculated by dividing the maximum output power density (P_{pv}) of the photovoltaic device by the total incoming power density from the solar spectrum, P_{solar}, as

$$\mathrm{PCE} = \frac{P_{pv}}{P_{solar}} \tag{1}$$

To ensure that our findings are fully reproducible,[63,64] transferable,[65,66] and compliant with the FAIR[67] data principles, we openly provide all key input files used

https://doi.org/10.1021/acs.jpcc.5c05620
J. Phys. Chem. C XXXX, XXX, XXX−XXX

Table 1. Equilibrium Structural Parameters of $AsNCa_3$ in Eight Different Polymorphs, Including the Number of Formula Units per Cell (Z), the Space Group (S.G.), Lattice Constants (a_0, b_0, and c_0), Relative Total Energy per Atom and by Formula Units per Cell (E_{rel}), Cohesive Energy per Atom (E_{coh}), ECN, and Average N−Ca Bond Length (DAV)[a]

phase	Z	S.G.	a_0 (Å)	b_0 (Å)	c_0 (Å)	$E_{relative}$ (eV/atom)	$E_{relative}$ (eV/Z)	E_{coh} (eV/atom)	ECN (N)	DAV (Å)
ideal cubic	1	$Pm\bar{3}m$	4.76	4.76	4.76	0.000	0.00	−3.883	6.000	2.380
super cubic	8	$P1$	9.53	9.53	9.53	−0.006	−0.030	−3.890	6.000	2.408
tetragonal	4	$P1$	6.72	6.72	9.57	−0.003	−0.015	−3.887	6.000	2.398
orthorhombic	4	$P1$	6.76	6.72	9.52	−0.003	−0.015	−3.887	6.000	2.395
black	4	$Pnma$	6.73	6.74	9.56	−0.006	−0.030	−3.890	6.000	2.410
yellow	4	$Pnma$	7.92	3.99	13.68	0.086	0.423	−3.798	5.495	2.474
2H hexagonal	2	$P6_3/m$	6.63	6.63	5.88	0.089	0.445	−3.795	6.000	2.325
4H hexagonal	4	$Cmc2_1$	6.71	6.71	11.30	0.035	0.175	−3.848	5.996	2.352

[a]Negative cohesive energies across all phases confirm favorable thermodynamic formation.

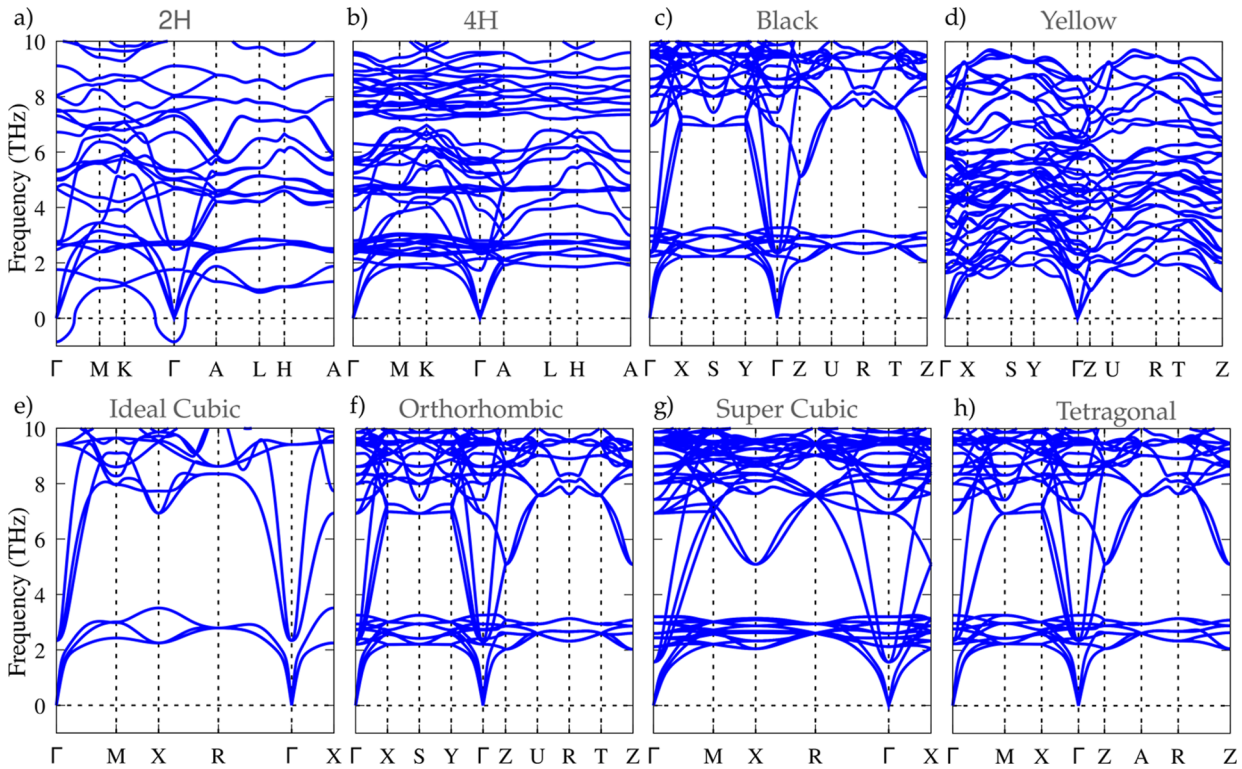

Figure 2. Phonon dispersions for eight $AsNCa_3$ antiperovskite polymorphs. Frequencies are given in terahertz (THz), and the path in the first Brillouin zone depends on the symmetry of each crystal. The figures are (a) 2H, (b) 4H, (c) black, (d) yellow, (e) ideal cubic, (f) orthorhombic, (g) super cubic, and (h) tetragonal.

throughout this work, including VASP, DFTB+, xTB, Wannier90, and WanTiBEXOS configurations, in a dedicated repository at https://github.com/ac-dias/AsNCa3-paper-raw-data. This archive also includes postprocessing scripts and auxiliary data, enabling straightforward verification and extension of the present results.

3. RESULTS

3.1. Stability and Structural Properties. The antiperovskite $AsNCa_3$ was examined in eight structural polymorphs, some of them previously identified by Dias et al.,[36] as illustrated in Figure 1. The number of formula units per cell (Z) varies by phase, as listed in Table 1. The assigned space groups are as follows: ideal cubic ($Pm\bar{3}m$); super cubic ($P1$, considered as a symmetry-lowered supercell of the cubic phase); $P1$ group for super-cubic, tetragonal, and orthorhombic phases; black and yellow phases (both in $Pnma$); 2H hexagonal ($P6_3/m$); and 4H hexagonal ($Cmc2_1$). Complete atomic positions are provided in Supporting Information. Table 1 reports equilibrium lattice parameters (a_0, b_0, and c_0), relative total energy per atom (E_{rel}), cohesive energies (E_{coh}), average N−Ca bond length (DAV), and effective coordination number (ECN). Note that ECN is calculated using a distance-weighted scheme (based on Hoppe's method)[68,69] to quantify the extent of octahedral distortion; values below 6 indicate deviations from ideal symmetry due to bond-length variation.

High-symmetry structures, namely, ideal cubic, supercubic, tetragonal, orthorhombic, and black, exhibit short energy differences (≤6 meV/atom) and nearly constant average N−Ca bond lengths (within ≈0.030 Å), compared to lower symmetry phases (yellow, 2H, and 4H hexagonal). These observations suggest that such phases may interconvert under environmental perturbations (phase transitions), including solar illumination (energy influx from solar radiation). The ECN of N, in the center of NCa_6 octahedra, reveals the

https://doi.org/10.1021/acs.jpcc.5c05620
J. Phys. Chem. C XXXX, XXX, XXX−XXX

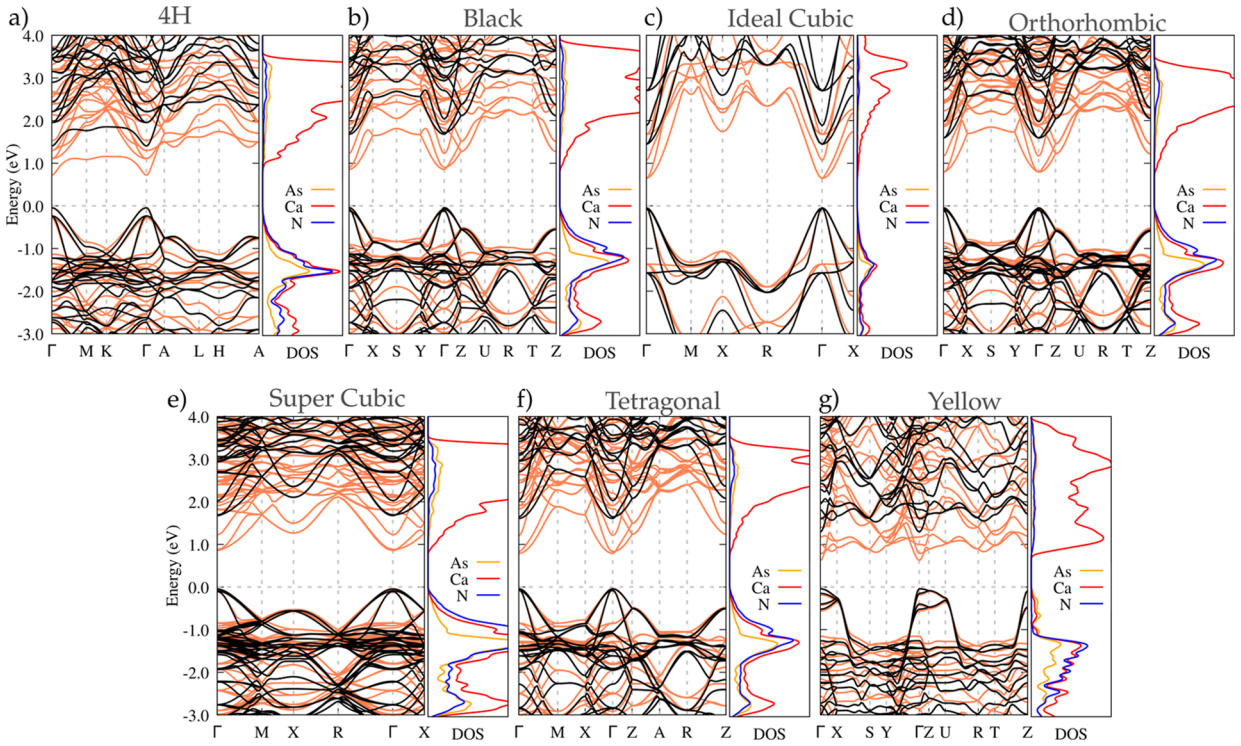

Figure 3. Band structures and DOS for $AsNCa_3$ antiperovskite polymorphs. The valence-band maximum has been shifted to 0 eV. Orange lines correspond to bands from PBE calculations and black lines to HSE06. The structures are (a) 4H, (b) black, (c) yellow, (d) ideal cubic, (e) orthorhombic, (f) super cubic, and (g) tetragonal.

octahedral distortion. More distorted structures exhibit ECN values lower than the ideal value of 6, such as 5.495 and 5.996 for yellow and 4H phases, respectively. Furthermore, negative cohesive energies across all polymorphs confirm exothermic formation and a favorable structural stability.

Phonon dispersion calculations were carried out to further evaluate the structural stability of the $AsNCa_3$ phases. As shown in Figure 2, for all polymorphs, the absence of imaginary frequencies across the Brillouin zone confirms the dynamical stability of all considered phases except for the 2H hexagonal phase, which exhibits negative (imaginary) phonon modes, indicative of dynamic instability. Based on these results, only dynamically stable phases were considered in the subsequent electronic and optical properties analyses.

3.2. Electronic Properties. The electronic properties were investigated through band structure and DOS calculations. All of the stable phases are presented in Figure 3. In all cases, the conduction band minimum predominantly comprises Ca atomic states, regardless of the structural phase. However, the nature of the valence band maximum (VBM) varies with symmetry. In the high-symmetry phases, ideal cubic, super cubic, tetragonal, and black, the VBM is primarily derived from N orbitals. In contrast, for lower-symmetry structures such as the yellow, 2H, and 4H hexagonal phases (represented by the yellow phase in Figure 3), the VBM is dominated by As orbitals. This shift in orbital character at the VBM is attributed to the symmetry breaking caused by octahedral distortions, which modify the local crystal field and orbital hybridization.[36]

As well-established and reported in the literature,[36,52,70,71] the PBE functional underestimates band gaps, while HSE06 predictions align more closely with experimental observations. Therefore, the band gaps predicted using HSE06, as presented in Table 2, are considered more reliable for these materials. All

Table 2. Band Gaps Computed with PBE (E_g^{PBE}) and HSE06 (E_g^{HSE06}), alongside Maximum Theoretical PCE (PCE^{SLME}) within the IPA and at T = 300 K

phase	E_g^{PBE} (eV)	E_g^{HSE06} (eV)	PCE^{SLME} (%)
ideal cubic	0.69	1.49	31.23
super cubic	0.90	1.72	27.50
tetragonal	0.83	1.65	28.84
orthorhombic	0.83	1.64	29.05
black	0.90	1.72	27.25
yellow	0.67	1.33	30.24
4H hexagonal	0.77	1.45	30.71

dynamically stable phases exhibit a direct band gap at the Γ-point, as illustrated in Figure 3. The computed gap values range from 1.33 to 1.72 eV, which falls within the optimal window (1.1−1.7 eV) for single-junction photovoltaic cells.[61] According to the Shockley−Queisser theory, the maximum theoretical efficiency occurs at a band gap near 1.34 eV[61] (under AM 1.5G illumination). Hence, solely on the basis of band gap alignment, all examined phases demonstrate promising prospects for solar cell applications. This behavior contrasts with that of many halide perovskites, where phase transitions can significantly alter the band gap. In contrast, the similar band gap values across all $AsNCa_3$ phases suggest that efficiency should remain stable even if phase conversions occur in response to environmental stimuli such as light or moisture.

3.3. Optical Properties and Application to Solar Cells. To further explore the optoelectronic behavior of $AsNCa_3$, we investigated its linear optical response via the absorption coefficient (Figure 4) for all dynamically stable polymorphs. We found that most polymorphs exhibit isotropic optical absorption, where the spectra for $\hat{x}$, $\hat{y}$, and $\hat{z}$ polarization

https://doi.org/10.1021/acs.jpcc.5c05620
J. Phys. Chem. C XXXX, XXX, XXX−XXX

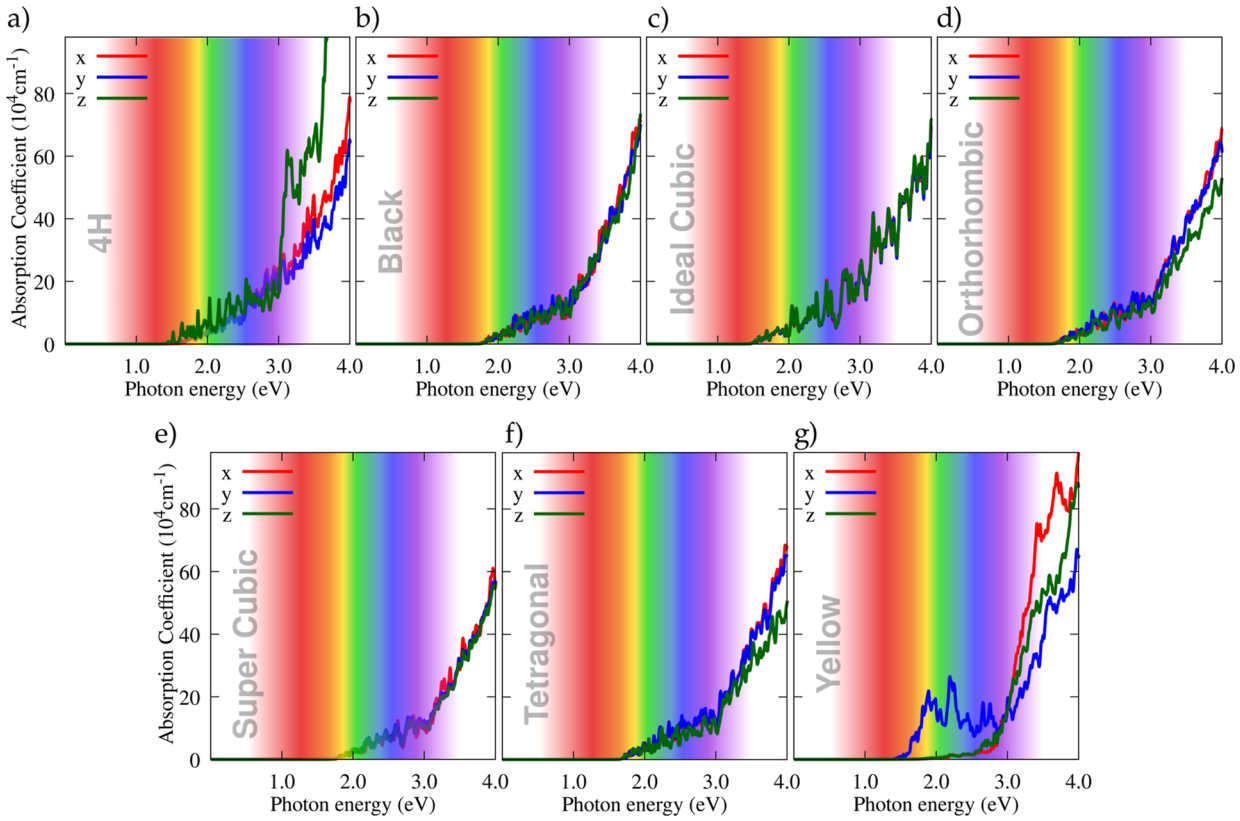

Figure 4. Comparison of the absorption coefficient for $AsNCa_3$ antiperovskite polymorphs. The plots show the linear absorption response under light polarized along the crystallographic directions $\hat{x}$ (red), $\hat{y}$ (blue), and $\hat{z}$ (green). The color bar highlights the visible spectrum range, within which the material exhibits strong optical absorption. The structures are (a) 4H, (b) black, (c) yellow, (d) ideal cubic, (e) orthorhombic, (f) super cubic, and (g) tetragonal.

(shown in red, blue, and green, respectively) are nearly identical. Conversely, the yellow phase displays optical anisotropy, reflecting its reduced symmetry, and absorption amplitudes vary notably across different polarizations in the visible range, as depicted in Figure 4. Detailed values of absorption coefficients, refractive indices (n), and reflectivity (R) for all stable phases are provided in the Supporting Information (Section S10).

To evaluate the PV potential of $AsNCa_3$, we calculated the PCE using the SLME model as a function of absorber layer thickness (Figure 5). Calculations were performed at 300 K within the IPA, considering film thicknesses up to 1 μm to minimize defect-mediated recombination. Table 2 summarizes the maximum SLME values. Among the polymorphs, the ideal cubic exhibits the highest PCE of 31.23%, while the black phase shows the lowest at 27.25%.

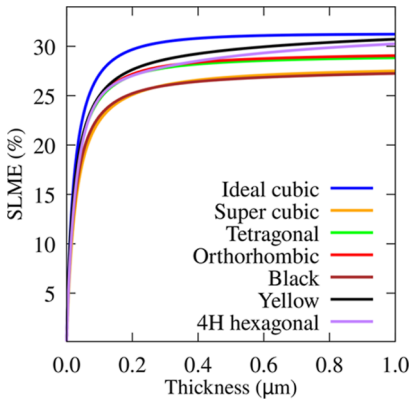

Figure 5. PCE^{SLME} versus $AsNCa_3$ antiperovskite thickness for all stable phases.

Despite the yellow phase band gap (1.33 eV) being very close to the Shockley–Queisser limit of 1.34 eV, it fails to reach the maximum SLME. This discrepancy arises from its optical anisotropy, an uneven absorption profile across polarizations, which reduces photon harvesting efficiency, particularly at lower energies. Nevertheless, increasing the film thickness to above 1 μm can partly mitigate this effect.

Importantly, all stable phases deliver SLME values near or above the theoretical limit for silicon single-junction cells (≈29%).[72] The consistency in high efficiencies across phases suggests that photovoltaic performance will remain largely unaffected by environment-driven phase transitions, such as those induced by light or moisture, even considering the lowest values in Table 2.

4. CONCLUSION

By analyzing the optoelectronic properties of $AsNCa_3$ antiperovskite polymorphs, we demonstrate their strong potential for single-junction solar-cell applications, achieving estimated SLME efficiencies near the theoretical maximum. Our findings also reveal that unlike many halide perovskites, whose band gaps and conversion efficiencies are significantly degraded by phase transitions, $AsNCa_3$ maintains consistent photovoltaic performance across all stable structural forms, with efficiencies closely tracking those of silicon (≈29%) and exceeding it in some cases. Nevertheless, the device's

https://doi.org/10.1021/acs.jpcc.5c05620
J. Phys. Chem. C XXXX, XXX, XXX−XXX

operational stability of $AsNCa_3$ over the long term must be investigated, particularly under conditions relevant to device deployment (e.g., exposure to moisture, ultraviolet light, and device-level electrical bias). What was learned from halide perovskite solar cells is the value of tailored passivation schemes and robust encapsulation for removing degradation mechanisms associated with environmental stressors and ionic migration. The same strategies, including grain boundaries, interfaces, and moisture barriers, will likely be required to realize the full potential of antiperovskite-based photovoltaics. These challenges must be overcome to translate the encouraging intrinsic properties of $AsNCa_3$ into high-performance, stable solar-cell devices.

■ ASSOCIATED CONTENT

Supporting Information

The Supporting Information is available free of charge at https://pubs.acs.org/doi/10.1021/acs.jpcc.5c05620.

PAW projectors, computational technical details; structural data in the POSCAR format; high symmetry **k**-points; phonon dispersions; thermodynamic properties; electronic band structure and projected DOS; computational parameters for optical properties, optical properties complementary data; and insights into solar harvesting efficiency (PDF)

■ AUTHOR INFORMATION

Corresponding Author

Alexandre C. Dias − *Institute of Physics and International Center of Physics, University of Brasília, 70919-970 Brasília, Distrito Federal, Brazil;* orcid.org/0000-0001-5934-8528; Email: alexandre.dias@unb.br

Authors

Muhammad Irfan − *Institute of Physics, University of Brasília, 70919-970 Brasília, Distrito Federal, Brazil; Computational Materials Laboratory, LCCMat, Institute of Physics, University of Brasília, 70919-970 Brasília, Distrito Federal, Brazil*

Bill D. Aparicio-Huacarpuma − *Institute of Physics, University of Brasília, 70919-970 Brasília, Distrito Federal, Brazil; Computational Materials Laboratory, LCCMat, Institute of Physics, University of Brasília, 70919-970 Brasília, Distrito Federal, Brazil*

Carlos M. de Oliveira Bastos − *Institute of Physics and International Center of Physics, University of Brasília, 70919-970 Brasília, Distrito Federal, Brazil*

Celso R. C. Rêgo − *Institute of Nanotechnology, Karlsruhe Institute of Technology (KIT), 76344 Eggenstein-Leopoldshafen, Baden-Württemberg, Germany;* orcid.org/0000-0003-1861-2438

Diego Guedes-Sobrinho − *Quantum Chemistry and Materials Thermodynamics Group, Q^2 M, Chemistry Department, Federal University of Paraná, 81531-980 Curitiba, Brazil;* orcid.org/0000-0002-3313-2822

Rafael Besse − *Institute of Physics and International Center of Physics, University of Brasília, 70919-970 Brasília, Distrito Federal, Brazil*

Maurício J. Piotrowski − *Department of Physics, Federal University of Pelotas, 96010-900 Pelotas, Rio Grande do Sul, Brazil;* orcid.org/0000-0003-3477-4437

Alysson M. Almeida Silva − *College of Technology, Department of Mechanical Engineering, University of Brasília, 70910-900 Brasília, Federal District, Brazil*

L. A. Ribeiro, Jr. − *Institute of Physics, University of Brasília, 70919-970 Brasília, Distrito Federal, Brazil; Computational Materials Laboratory, LCCMat, Institute of Physics, University of Brasília, 70919-970 Brasília, Distrito Federal, Brazil;* orcid.org/0000-0001-7468-2946

Complete contact information is available at: https://pubs.acs.org/10.1021/acs.jpcc.5c05620

Funding

The Article Processing Charge for the publication of this research was funded by the Coordenacao de Aperfeicoamento de Pessoal de Nivel Superior (CAPES), Brazil (ROR identifier: 00x0ma614).

Notes

The authors declare no competing financial interest.

■ ACKNOWLEDGMENTS

Authors thank the Rio Grande do Sul Research Foundation (FAPERGS, grant 24/2551-0001551-5), the Federal District Research Support Foundation (FAPDF, grants 00193-00001817/2023-43 and 00193-00002073/2023-84), the National Council for Scientific and Technological DevelopmentCNPq (307345/2021-1, 408144/2022-0, 305174/2023-1, 444431/2024-1, 141176/2024-5, and 444069/2024-0), and the Coordination for Improvement of Higher Level EducationCAPES (finance Code 001) for the financial support. C.R.C.R. thanks the German Federal Ministry of Education and Research (BMBF) for financial support of the project Innovation-Platform MaterialDigital (www.materialdigital.de) through project funding FKZ number: 13XP5094A. Part of this work was performed on the HoreKa supercomputer funded by the Ministry of Science, Research and the Arts Baden-Württemberg and by the Federal Ministry of Education and Research. This work also used resources of the "Centro Nacional de Processamento de Alto Desempenho em São Paulo" (CENAPAD-SP, UNICAMP/FINEP-MCTI), projects 897 and 570; of the "Centro Nacional de Supercomputação (CESUP-UFRGS)"; of the Lobo Carneiro HPC (NACAD) at the Federal University of Rio de Janeiro, from project 133; of the Ogun supercomputer of the CIMATEC SENAI at Salvador-BA; of the SDumont supercomputer in the Laboratório Nacional de Computação Científica (LNCC) at Petrópolis-RJ, as part of the "Sistema Nacional de Processamento de Alto Desempenho"—SINAPAD; and of the "Laboratório Central de Processamento de Alto Desempenho" (LCPAD), financed by FINEP through CT-INFRA/UFPR projects. A.C.D. and L.A.R.J. acknowledge PDPG-FAPDF-CAPES Centro-Oeste 00193-00000867/2024-94. L.A.R.J. acknowledges the financial support from FAP-DF grants 00193.00001808/2022-71 and 00193-00001857/2023-95, FAPDF-PRONEM grant 00193.00001247/2021-20, and CNPq grants 350176/2022-1, 167745/2023-9, 444111/2024-7. This paper was published under the CC BY Open Access license through the ACS-CAPES agreement. The authors gratefully acknowledge CAPES for the financial support provided for the publication of this work under the ACS-CAPES agreement.

REFERENCES

(1) Rani, U.; Kamlesh, P. K.; Shukla, A.; Verma, A. S. Emerging potential antiperovskite materials ANX3 (A= P, As, Sb, Bi; X= Sr, Ca, Mg) for thermoelectric renewable energy generators. *J. Solid State Chem.* **2021**, *300*, 122246.

(2) Ali, R.; Hou, G.-J.; Zhu, Z.-G.; Yan, Q.-B.; Zheng, Q.-R.; Su, G. Predicted Lead-Free Perovskites for Solar Cells. *Chem. Mater.* **2018**, *30*, 718−728.

(3) Dong, Q.; Fang, Y.; Shao, Y.; Mulligan, P.; Qiu, J.; Cao, L.; Huang, J. Electron-hole diffusion lengths > 175 μm in solution-grown $CH_3NH_3PbI_3$ single crystals. *Science* **2015**, *347*, 967−970.

(4) Yin, W.-J.; Yang, J.-H.; Kang, J.; Yan, Y.; Wei, S.-H. Halide perovskite materials for solar cells: a theoretical review. *J. Mater. Chem. A* **2015**, *3*, 8926−8942.

(5) Sajid, S.; Alzahmi, S.; Salem, I. B.; Tabet, N.; Haik, Y.; Obaidat, I. M. Desirable candidates for high-performance lead-free organic−inorganic halide perovskite solar cells. *Mater. Renew. Sustain. Energy* **2024**, *13*, 133−153.

(6) Fan, X. Advanced progress in metal halide perovskite solar cells: A review. *Mater. Today Sustain.* **2023**, *24*, 100603.

(7) Meng, Q.; Chen, Y.; Xiao, Y. Y.; Sun, J.; Zhang, X.; Han, C. B.; Gao, H.; Zhang, Y.; Yan, H. Effect of temperature on the performance of perovskite solar cells. *J. Mater. Sci.: Mater. Electron.* **2021**, *32*, 12784−12792.

(8) Araujo, L. O. d.; Rêgo, C. R.; Wenzel, W.; Bastos, C. M. d. O.; Piotrowski, M. J.; Dias, A. C.; Guedes-Sobrinho, D. Thermodynamic modeling and electronic properties of CsPb1-xSnxI3 as a polymorphic alloy. *J. Alloys Compd.* **2024**, *992*, 174485.

(9) Nie, W.; Blancon, J.-C.; Neukirch, A. J.; Appavoo, K.; Tsai, H.; Chhowalla, M.; Alam, M. A.; Sfeir, M. Y.; Katan, C.; Even, J.; et al. Light-activated photocurrent degradation and self-healing in perovskite solar cells. *Nat. Commun.* **2016**, *7*, 11574.

(10) Octavio de Araujo, L.; Rêgo, C. R. C.; Wenzel, W.; Sabino, F. P.; Guedes-Sobrinho, D. Impact of the Polymorphism and Relativistic Effects on the Electronic Properties of Inorganic Metal Halide Perovskites. *J. Phys. Chem. C* **2022**, *126*, 2131−2140.

(11) Mesquita, I.; Andrade, L.; Mendes, A. Effect of relative humidity during the preparation of perovskite solar cells: Performance and stability. *Sol. Energy* **2020**, *199*, 474−483.

(12) Idigoras, J.; Aparicio, F. J.; Contreras-Bernal, L.; Ramos-Terrón, S.; Alcaire, M.; Sánchez-Valencia, J. R.; Borras, A.; Barranco, A.; Anta, J. A. Enhancing Moisture and Water Resistance in Perovskite Solar Cells by Encapsulation with Ultrathin Plasma Polymers. *ACS Appl. Mater. Interfaces* **2018**, *10*, 11587−11594.

(13) Afre, R. A.; Pugliese, D. Perovskite Solar Cells: A Review of the Latest Advances in Materials, Fabrication Techniques, and Stability Enhancement Strategies. *Micromachines* **2024**, *15*, 192.

(14) Guedes-Sobrinho, D.; Neves Silveira, D.; de Araujo, L. O.; Favotto Dalmedico, J.; Wenzel, W.; Pramudya, Y.; Piotrowski, M. J.; Rêgo, C. R. C. Revealing the impact of organic spacers and cavity cations on quasi-2D perovskites via computational simulations. *Sci. Rep.* **2023**, *13*, 4446.

(15) Silveira, D. N.; Dias, A. C.; Araujo, L. O. d.; Queiroz, M. A.; Dalmedico, J. F.; Bastos, C. M. d. O.; Rêgo, C. R. C.; Piotrowski, M. J.; Guedes-Sobrinho, D. Excitonic properties and solar harvesting performance of Cs2ZnY2X2 as quasi-2D mixed-halide perovskites. *J. Alloys Compd.* **2024**, *1007*, 176434.

(16) Dalmedico, J. F.; Silveira, D. N.; O de Araujo, L.; Wenzel, W.; Rêgo, C. R. C.; Dias, A. C.; Guedes-Sobrinho, D.; Piotrowski, M. J. Tuning Electronic and Structural Properties of Lead-Free Metal Halide Perovskites: A Comparative Study of 2D Ruddlesden-Popper and 3D Compositions. *ChemPhysChem* **2024**, *25*, No. e202400118.

(17) Rêgo, C. R. C.; Wenzel, W.; Piotrowski, M. J.; Dias, A. C.; Maciel de Oliveira Bastos, C.; de Araujo, L. O.; Guedes-Sobrinho, D. Digital workflow optimization of van der Waals methods for improved halide perovskite solar materials. *Digital Discovery* **2025**, *4*, 927−942.

(18) Zhang, X.; Chen, X.; Chen, Y.; Nadege Ouedraogo, N. A.; Li, J.; Bao, X.; Han, C. B.; Shirai, Y.; Zhang, Y.; Yan, H. Rapid degradation behavior of encapsulated perovskite solar cells under light, bias voltage or heat fields. *Nanoscale Adv.* **2021**, *3*, 6128−6137.

(19) Du, Y.; Wan, S.; Xie, M.; Xia, Y.; Yang, W.; Wei, Z.; Zhu, Y.; Hua, Y.; Jin, Z.; Hong, D.; et al. Electric-Field-Induced Ion Migration Behavior in Methylammonium Lead Iodide Perovskite. *J. Phys. Chem. Lett.* **2021**, *12*, 7106−7112.

(20) Bae, S.; Kim, S.; Lee, S.-W.; Cho, K. J.; Park, S.; Lee, S.; Kang, Y.; Lee, H.-S.; Kim, D. Electric-Field-Induced Degradation of Methylammonium Lead Iodide Perovskite Solar Cells. *J. Phys. Chem. Lett.* **2016**, *7*, 3091−3096.

(21) Eperon, G. E.; Paternò, G. M.; Sutton, R. J.; Zampetti, A.; Haghighirad, A. A.; Cacialli, F. o.; Snaith, H. J. Inorganic caesium lead iodide perovskite solar cells. *J. Mater. Chem. A* **2015**, *3*, 19688−19695.

(22) Protesescu, L.; Yakunin, S.; Bodnarchuk, M. I.; Krieg, F.; Caputo, R.; Hendon, C. H.; Yang, R. X.; Walsh, A.; Kovalenko, M. V. Nanocrystals of Cesium Lead Halide Perovskites (CsPbX3, X = Cl, Br, and I): Novel Optoelectronic Materials Showing Bright Emission with Wide Color Gamut. *Nano Lett.* **2015**, *15*, 3692−3696.

(23) Waleed, A.; Tavakoli, M. M.; Gu, L.; Hussain, S.; Zhang, D.; Poddar, S.; Wang, Z.; Zhang, R.; Fan, Z. All Inorganic Cesium Lead Iodide Perovskite Nanowires with Stabilized Cubic Phase at Room Temperature and Nanowire Array-Based Photod etectors. *Nano Lett.* **2017**, *17*, 4951−4957.

(24) Swarnkar, A.; Marshall, A. R.; Sanehira, E. M.; Chernomordik, B. D.; Moore, D. T.; Christians, J. A.; Chakrabarti, T.; Luther, J. M. Quantum dot−induced phase stabilization of α-$CsPbI_3$ perovskite for high-efficiency photovoltaics. *Science* **2016**, *354*, 92−95.

(25) Bhatt, H.; Saha, R.; Goswami, T.; C, K. S.; Justice Babu, K.; Kaur, G.; Shukla, A.; Patel, M. S.; Rondiya, S. R.; Dzade, N. Y.; et al. Charge Transfer Modulation in the α-$CsPbI_3/WS_2$ Heterojunction via Band-Tailoring with Elemental Ni Doping. *ACS Photonics* **2024**, *11*, 5367−5379.

(26) Nigmetova, G.; Yelzhanova, Z.; Zhumadil, G.; Parkhomenko, H. P.; Tilegen, M.; Zhou, X. n.; Pavlenko, V.; Beisenbayev, A.; Aidarkhanov, D.; Jumabekov, A. N.; et al. Controlling the Growth of Cs_2PbX_4 Nanostructures Enhances the Stability of Inorganic Cesium-Based Perovskite Solar Cells for Potentia l Low Earth Orbit Applications. *ACS Appl. Mater. Interfaces* **2025**, *17*, 31575−31591.

(27) Wang, B.; Novendra, N.; Navrotsky, A. Energetics, Structures, and Phase Transitions of Cubic and Orthorhombic Cesium Lead Iodide (CsPbI3) Polymorphs. *J. Am. Chem. Soc.* **2019**, *141*, 14501−14504.

(28) Lyu, H.; Su, H.; Lin, Z. Two-Stage Dynamic Transformation from δ- to α-CsPbI3. *J. Phys. Chem. Lett.* **2024**, *15*, 2228−2232.

(29) Ke, F.; Wang, C.; Jia, C.; Wolf, N. R.; Yan, J.; Niu, S.; Devereaux, T. P.; Karunadasa, H. I.; Mao, W. L.; Lin, Y. Preserving a robust CsPbI3 perovskite phase via pressure-directed octahedral tilt. *Nat. Commun.* **2021**, *12*, 461.

(30) Ke, F.; Yan, J.; Niu, S.; Wen, J.; Yin, K.; Yang, H.; Wolf, N. R.; Tzeng, Y.-K.; Karunadasa, H. I.; Lee, Y. S.; et al. Cesium-mediated electron redistribution and electron-electron interaction in high-pressure metallic CsPbI3. *Nat. Commun.* **2022**, *13*, 7067.

(31) He, T.; Huang, Q.; Ramirez, A. P.; Wang, Y.; Regan, K. A.; Rogado, N.; Hayward, M. A.; Haas, M. K.; Slusky, J. S.; Inumara, K.; et al. Superconductivity in the non-oxide perovskite MgCNi3. *Nature* **2001**, *411*, 54−56.

(32) Kim, W.; Chi, E.; Kim, J.; Choi, H.; Hur, N. Close correlation among lattice, spin, and charge in the manganese-based antiperovskite material. *Solid State Commun.* **2001**, *119*, 507−510.

(33) Hamada, T.; Takenaka, K. Giant negative thermal expansion in antiperovskite manganese nitrides. *J. Appl. Phys.* **2011**, *109*, 07E309.

(34) Hassan, M.; Arshad, I.; Mahmood, Q. Computational study of electronic, optical and thermoelectric properties of X3PbO (X = Ca, Sr, Ba) anti-perovskites. *Semicond. Sci. Technol.* **2017**, *32*, 115002.

(35) Wang, Y.; Zhang, H.; Zhu, J.; Lü, X.; Li, S.; Zou, R.; Zhao, Y. Antiperovskites with Exceptional Functionalities. *Adv. Mater.* **2020**, *32*, 1905007.

(36) Dias, A. C.; Lima, M. P.; Da Silva, J. L. F. Role of Structural Phases and Octahedra Distortions in the Optoelectronic and

https://doi.org/10.1021/acs.jpcc.5c05620
J. Phys. Chem. C XXXX, XXX, XXX−XXX

Excitonic Properties of CsGeX3 (X = Cl, Br, I) Perovskites. *J. Phys. Chem. C* **2021**, *125*, 19142−19155.
(37) Goh, W. F.; Pickett, W. E. Topological and thermoelectric properties of double antiperovskite pnictides. *J. Phys.: Condens. Matter* **2020**, *32*, 345502.
(38) Ma, X.; Liu, C.; Materzanini, G.; Rignanese, G.-M.; Ren, W. Ferroelectricity, triple-well potential, and negative piezoelectricity in the antiperovskite γ-Ag_3SI. *Phys. Rev. B* **2024**, *110*, 184109.
(39) Feng, C.; Wu, C.; Luo, X.; Hu, T.; Chen, F.; Li, S.; Duan, S.; Hou, W.; Li, D.; Tang, G.; et al. Pressure-dependent electronic, optical, and mechanical properties of antiperovskite X3NP (X = Ca, Mg): A first-principles study. *J. Semicond.* **2023**, *44*, 102101.
(40) Hu, T.; Wu, C.; Li, M.; Qu, H.; Luo, X.; Hou, Y.; Li, S.; Duan, S.; Li, D.; Tang, G.; et al. Pressure-dependent optoelectronic properties of antiperovskite derivatives X3AsCl3 (X = Mg, Ca, Sr, Ba): a first-principles study. *Phys. Chem. Chem. Phys.* **2025**, *27*, 4144−4151.
(41) Tong, P.; Sun, Y.; Zhao, B.; Zhu, X.; Song, W. Influence of carbon concentration on structural, magnetic and electrical transport properties for antiperovskite compounds AlCxMn3. *Solid State Commun.* **2006**, *138*, 64−67.
(42) Kresse, G.; Hafner, J. Ab initiomolecular dynamics for open-shell transition metals. *Phys. Rev. B: Condens. Matter Mater. Phys.* **1993**, *48*, 13115−13118.
(43) Kresse, G.; Furthmüller, J. Efficient iterative schemes forab initiototal-energy calculations using a plane-wave basis set. *Phys. Rev. B: Condens. Matter Mater. Phys.* **1996**, *54*, 11169−11186.
(44) Kohn, W.; Sham, L. J. Self-Consistent Equations Including Exchange and Correlation Effects. *Phys. Rev.* **1965**, *140*, A1133−A1138.
(45) Hohenberg, P.; Kohn, W. Inhomogeneous electron gas. *Phys. Rev.* **1964**, *136*, B864.
(46) Kresse, G.; Joubert, D. From ultrasoft pseudopotentials to the projector augmented-wave method. *Phys. Rev. B: Condens. Matter Mater. Phys.* **1999**, *59*, 1758−1775.
(47) Perdew, J. P.; Burke, K.; Ernzerhof, M. Generalized Gradient Approximation Made Simple. *Phys. Rev. Lett.* **1996**, *77*, 3865−3868.
(48) Cohen, A. J.; Mori-Sánchez, P.; Yang, W. Fractional charge perspective on the band gap in density-functional theory. *Phys. Rev. B: Condens. Matter Mater. Phys.* **2008**, *77*, 115123.
(49) Crowley, J. M.; Tahir-Kheli, J.; Goddard, W. A. Resolution of the Band Gap Prediction Problem for Materials Design. *J. Phys. Chem. Lett.* **2016**, *7*, 1198−1203.
(50) Heyd, J.; Scuseria, G. E.; Ernzerhof, M. Hybrid functionals based on a screened Coulomb potential. *J. Chem. Phys.* **2003**, *118*, 8207−8215.
(51) Krukau, A. V.; Vydrov, O. A.; Izmaylov, A. F.; Scuseria, G. E. Influence of the exchange screening parameter on the performance of screened hybrid functionals. *J. Chem. Phys.* **2006**, *125*, 224106.
(52) Bastos, C. M.; Sabino, F. P.; Sipahi, G. M.; Da Silva, J. L. F. A comprehensive study of g -factors, elastic, structural and electronic properties of III-V semiconductors using hybrid-density functional theory. *J. Appl. Phys.* **2018**, *123*, 065702.
(53) Pela, R. R.; Hsiao, C.-L.; Hultman, L.; Birch, J.; Gueorguiev, G. K. Electronic and optical properties of core−shell InAlN nanorods: a comparative study via LDA, LDA-1/2, mBJ, HSE06, G0W0 and BSE methods. *Phys. Chem. Chem. Phys.* **2024**, *26*, 7504−7514.
(54) Togo, A.; Tanaka, I. First principles phonon calculations in materials science. *Scr. Mater.* **2015**, *108*, 1−5.
(55) Hourahine, B.; Aradi, B.; Blum, V.; Bonafé, F.; Buccheri, A.; Camacho, C.; Cevallos, C.; Deshaye, M. Y.; Dumitrică, T.; Dominguez, A.; et al. DFTB+, a software package for efficient approximate density functional theory based atomistic simulations. *J. Chem. Phys.* **2020**, *152*, 124101.
(56) Bannwarth, C.; Caldeweyher, E.; Ehlert, S.; Hansen, A.; Pracht, P.; Seibert, J.; Spicher, S.; Grimme, S. Extended tight-binding quantum chemistry methods. *Wiley Interdiscip. Rev. Comput. Mol. Sci.* **2021**, *11* (11), No. e1493.
(57) Grimme, S.; Bannwarth, C.; Shushkov, P. A Robust and Accurate Tight-Binding Quantum Chemical Method for Structures, Vibrational Frequencies, and Noncovalent Interactions of Large Molecular Systems Parametrized for All spd-Block Elements (Z = 1−86). *J. Chem. Theory Comput.* **2017**, *13*, 1989−2009.
(58) Vicent-Luna, J. M.; Apergi, S.; Tao, S. Efficient Computation of Structural and Electronic Properties of Halide Perovskites Using Density Functional Tight Binding: GFN1-xTB Method. *J. Chem. Inf. Model.* **2021**, *61*, 4415−4424.
(59) Dias, A. C.; Silveira, J. F.; Qu, F. WanTiBEXOS: A Wannier based Tight Binding code for electronic band structure, excitonic and optoelectronic properties of solids. *Comput. Phys. Commun.* **2023**, *285*, 108636.
(60) Mostofi, A. A.; Yates, J. R.; Lee, Y.-S.; Souza, I.; Vanderbilt, D.; Marzari, N. wannier90: A tool for obtaining maximally-localised Wannier functions. *Comput. Phys. Commun.* **2008**, *178*, 685−699.
(61) Yu, L.; Zunger, A. Identification of Potential Photovoltaic Absorbers Based on First-Principles Spectroscopic Screening of Materials. *Phys. Rev. Lett.* **2012**, *108*, 068701.
(62) *ASTM-G173-03 Standard Tables for Reference Solar Spectral Irradiances: Direct Normal and Hemispherical on 37° Tilted Surface*; ASTM International: West Conshohocken, PA, 2012.
(63) Bekemeier, S.; Caldeira Rêgo, C. R.; Mai, H. L.; Saikia, U.; Waseda, O.; Apel, M.; Arendt, F.; Aschemann, A.; Bayerlein, B.; Courant, R.; et al. Advancing Digital Transformation in Material Science: The Role of Workflows Within the MaterialDigital Initiative. *Adv. Eng. Mater.* **2025**, *27*, 2402149.
(64) Mostaghimi, M.; Rêgo, C. R. C.; Haldar, R.; Wöll, C.; Wenzel, W.; Kozlowska, M. Automated Virtual Design of Organic Semiconductors Based on Metal-Organic Frameworks. *Front. Mater.* **2022**, *9*, 840644.
(65) Rêgo, C. R. C.; Schaarschmidt, J.; Schlöder, T.; Penaloza-Amion, M.; Bag, S.; Neumann, T.; Strunk, T.; Wenzel, W. SimStack: An Intuitive Workflow Framework. *Front. Mater.* **2022**, *9*, 877597.
(66) Soleymanibrojeni, M.; Caldeira Rego, C. R.; Esmaeilpour, M.; Wenzel, W. An active learning approach to model solid-electrolyte interphase formation in Li-ion batteries. *J. Mater. Chem. A* **2024**, *12*, 2249−2266.
(67) Schaarschmidt, J.; Yuan, J.; Strunk, T.; Kondov, I.; Huber, S. P.; Pizzi, G.; Kahle, L.; Bölle, F. T.; Castelli, I. E.; Vegge, T.; et al. Workflow Engineering in Materials Design within the BATTERY 2030+ Project. *Adv. Energy Mater.* **2022**, *12*, 2102638.
(68) Hoppe, R. The Coordination Number − an "Inorganic Chameleon". *Angew. Chem., Int. Ed.* **1970**, *9*, 25−34.
(69) Hoppe, R. Effective Coordination Numbers (ECoN) and Mean Active Fictive Ionic Radii (MEFIR). *Z. Kristallogr.* **1979**, *150*, 23−52.
(70) Dias, A. C.; Bragança, H.; de Mendonça, J. P. A.; Da Silva, J. L. F. Excitonic Effects on Two-Dimensional Transition-Metal Dichalcogenide Monolayers: Impact on Solar Cell Efficiency. *ACS Appl. Energy Mater.* **2021**, *4*, 3265−3278.
(71) Bastos, C. M.; Besse, R.; Da Silva, J. L. F.; Sipahi, G. M. Ab initio investigation of structural stability and exfoliation energies in transition metal dichalcogenides based on Ti-V-and Mo-group elements. *Phys. Rev. Mater.* **2019**, *3*, 044002.
(72) Tiedje, T.; Yablonovitch, E.; Cody, G.; Brooks, B. Limiting efficiency of silicon solar cells. *IEEE Trans. Electron Devices* **1984**, *31*, 711−716.

https://doi.org/10.1021/acs.jpcc.5c05620
J. Phys. Chem. C XXXX, XXX, XXX−XXX